Self-Assembled Colloidal Crystals from ZrO_2 Nanoparticles

Jonathan D. Woodward,[†] Joseph M. Pickel,[‡] Lawrence M. Anovitz,[†] William T. Heller,[†] and Adam J. Rondinone*[,†,‡]

Chemical Sciences Division and Center for Nanophase Materials Sciences, Oak Ridge National Laboratory, Oak Ridge, Tennessee 37831

Received: April 21, 2006; In Final Form: July 24, 2006

Ordered three-dimensional (3-D) assemblies of nanocrystalline zirconia were synthesized from aqueous suspensions of ZrO_2 nanoparticles without the need for hydrocarbon surfactants or solvents to control colloidal crystal growth. Nanoparticles were suspended in mild acid and subsequently titrated from low to neutral pH. The solubility was reduced as the surfaces were neutralized, promoting assembly of the nanoparticles into ordered monoliths. TEM measurements indicated the formation of three-dimensional, hexagonal faceted, micrometer-sized colloidal crystals composed of 4 nm diameter ZrO_2 nanoparticles. Lacking organic surfactants, the colloidal crystals were exceptionally robust and were sintered at high temperatures (300−500 °C) for further stability. Small-angle X-ray scattering (SAXS) measurements demonstrate that the samples become progressively more amorphous above 350 °C, although some ordered domains of nanoparticles persist. Additionally, the heat treatment dramatically increases the surface area of the colloidal crystals as water and residual organics are desorbed, revealing highly controlled interstitial spaces and pores.

Introduction

Science at the nanoscale level has been the focus of considerable research efforts over the past decade aimed at producing materials with structural, optical, electronic, and magnetic properties not observed in discrete molecules or bulk solids. As in atomic and molecular entities, nanoparticles (NPs) can assemble to form well-ordered and close-packed solids, or colloidal crystals, that may possess novel and potentially useful collective physical properties.[1] The structure of any colloidal crystal is influenced by the size, morphology, and surface chemistry of the nanoparticle components. For example, colloidal crystals assembled from spherically monodisperse nanoparticles adopt a hexagonally close-packed (HCP) crystal structure while two-component nanoparticle systems usually adopt lower cubic AB_2 and AB_{13} symmetries.[2,3] Furthermore, the identity, arrangement, and bonding interactions between the nanoparticle components may influence the physical properties of colloidal crystals, although these structure−property relationships have not been investigated.

To date, most colloidal crystals have been grown from organic-capped nanoparticles dispersed in nonpolar solvents. On evaporation of the solvents, the hydrophobic nanoparticles are attracted by van der Waals forces and assemble into ordered superlattices.[2−4] For example, cubic colloidal crystals have been grown from spherical micrometer-sized poly(methyl methacrylate) particles.[5,6] Also, HCP colloidal crystals have been assembled from monodisperse SiO_2, $FePt/Fe_3O_4$, and CdSe nanoparticles,[1,7−9] and more complex orthorhombic and hexagonal superlattices composed of PbSe/Ag and PbSe/Pd nanocomposites have been reported.[10]

Alternatively, exploiting surface chemistry to assemble nanoparticles into ordered monoliths by maximizing ionic attractions or minimizing repulsions may produce more physically or thermally stable materials; this method is, however, virtually unexplored.[11−13] For example, single-component colloidal crystals can be grown by assembling surface-neutralized nanoparticles while dual component systems could be formed by attraction of charged nanoparticles to other oppositely charged nanoparticles.[13] Furthermore, by eliminating the organic molecules present on the NP surfaces, crystalline order may be retained or even enhanced upon heat treatment and sintering. Employing the concept of ionic surface charge, this paper reports the synthesis and characterization of micrometer-sized colloidal crystals assembled from ∼4 nm diameter ZrO_2 nanoparticles. These monoliths are grown in water without the use of surfactants or organic solvents and are stable up to 350 °C. Above 350 °C they become somewhat amorphous while still retaining some ordered colloidal crystal domains. Zirconia nanoparticles were chosen for this study because of their facile synthesis,[14] well-documented surface chemistry, high-temperature stability, and useful technological applications.[15,16]

Experimental Section

Multigram quantities of ZrO_2 nanoparticles were synthesized by the combination of zirconium(IV) isopropoxide with zirconium(IV) chloride via a nonhydrolytic sol−gel process at 340 °C (99% TOPO (Aldrich) was substituted for technical grade).[14] Transmission electron microscopy measurements identified monodisperse, approximately 4 nm diameter nanoparticles.[14] Powder X-ray diffraction measurements confirmed that the nanoparticles were tetragonal ZrO_2.[14,17] Upon isolation and purification, the tri-*n*-octylphosphine oxide (TOPO) surfactant was removed by refluxing the zirconia nanoparticles at 85 °C for 1 h in 50 mL of a 70%/30% (by volume) ethanol/water mixture, adjusted to pH = 2 by addition of concentrated sulfuric acid. The product was then washed twice with acetone and dispersed in 200 mL of deionized water. The pH of the nanoparticle suspension, initially 3.25, was raised to 7 by careful

* To whom correspondence should be addressed. Phone: (865) 574-5035. Fax: (865) 574-4961. E-mail: rondinoneaj@ornl.gov.
† Chemical Sciences Division.
‡ Center for Nanophase Materials Sciences.

10.1021/jp062471z CCC: $33.50
Published on Web 09/12/2006

dropwise addition of a 0.033 M KOH solution. No visible change in color or cloudiness occurred as the pH increased. The particles were stirred at room temperature for 24 h with the periodic addition of KOH to maintain the pH at 7. The product was then washed three times. Portions of the precipitate were dried in air and heat-treated at 250, 300, 350, 400, and 500 °C for 24 h. After heat treatment, the particles were found to lose 5−10% of the original mass. After heat treatment, the colloidal crystals are rendered insoluble and do not redissolve in water.

Colloidal crystal size and morphology were examined using both a Hitachi HF-2000 transmission electron microscope and a Hitachi HD-2000 scanning transmission electron microscope (STEM, probe size ca. 0.3 nm) operating at 200 keV. Samples for TEM were prepared by dispersing a small quantity of sample into methanol. A drop of dispersed sample was then placed on a carbon coated copper TEM grid (300 mesh). The TEM grid was allowed to dry before measurement. Wide-angle X-ray diffraction was performed using a Bruker D5005 goniometer using Cu $K\alpha_{1,2}$ radiation ($\lambda = 1.54$ Å) at 1600 W and operating at 40 keV and 40 mA. For wide-angle X-ray analysis, high temperature in situ heating was performed using a Parr HTK-16 furnace stage with the sample mounted on a Pt heating element.

Thermogravimetric analysis (TGA) was performed using a TA Instruments TGA 2050 connected to a Balzers Thermostar mass spectrometer via a 1 m long transfer line maintained at 200 °C. A 20 mg sample contained within an open ceramic pan was heated to 900 °C at a ramping rate of 10 °C/min under an argon atmosphere. The desorbed gases and materials were analyzed between 10 and 130 amu.

Specific surface area and pore size distribution were determined by N_2 absorption/desorption isotherms using a Quatasorb Autosorb system (Quantachrome Corp.) and standard multipoint Brunauer−Emmett−Teller (BET) analysis methods. Samples were degassed at 383 K for 3 h before N_2 physisorption measurements.

Small-angle X-ray scattering (SAXS) data were collected using the ORNL Center for Structural Molecular Biology 4m SAXS instrument, which employs a Rigaku rotating anode X-ray generator operating at 40 kV and 60 mA equipped with a Cu anode (Cu K_α radiation, $\lambda = 1.542$ Å) and a Ni filter at the exit port to reduce spectral contamination from Cu K_β radiation. Collimation was achieved using a pair of quartz mirrors that focus the X-rays at the plane of the detector. The samples were positioned approximately 2 m from the source and the scattered X-rays are collected with an Ordela 2201X position sensitive area detector (Oak Ridge, TN) located approximately 2 m from the sample. The precise detector distance was calibrated using cholesteryl myristate.

Data reduction was performed on a pixel by pixel basis and included corrections for variations in detector sensitivity, as determined using an ^{55}Fe source, dark current, and instrumental background according to eq 1

$$I(x,y) = \frac{1000.0}{t_S dA}\left[\left(S(x,y) - \frac{t_S}{t_{DC}}DC(x,y)\right) - \frac{t_S T_S}{t_B T_B}\left(B(x,y) - \frac{t_B}{t_{DC}}DC(x,y)\right)\right] \quad (1)$$

which is a modification of the previously reported expression.[18,19] In this equation, $S(x,y)$, $B(x,y)$, and $DC(x,y)$ are the measured sample, background, and dark current patterns, t_S, t_B, and t_{DC} are the measurements times, and T_S and T_B are the measured transmissions of the sample and background materials, respectively. The leading term takes into account a scaling factor (1000.0), the sample thickness, d, and an additional absolute scaling factor, A, which is determined using a precalibrated standard, that provides the reduced intensity as an absolute cross-section.[19] As the instrument lacks a beam monitor to measure the incident intensity, this correction is omitted from eq 1. Instead, the relative normalization of $S(x,y)$ and $B(x,y)$ is performed using the measurement times. After subtraction, data were azimuthally averaged to produce a one-dimensional profile, $I(q)$ versus q, where $q = 4\pi \sin(\theta)/\lambda$, 2θ is the scattering angle from the incident beam, and λ is the wavelength. For strongly scattering samples, the useful q-range of the instrument is approximately 0.01−0.36 Å^{-1}. Powdered samples were situated between two pieces of clear packing tape, and the sample thickness was measured with a micrometer. Measurement times for both the samples and tape background were 30 min. Samples transmissions were determined using glassy carbon as described previously.[18]

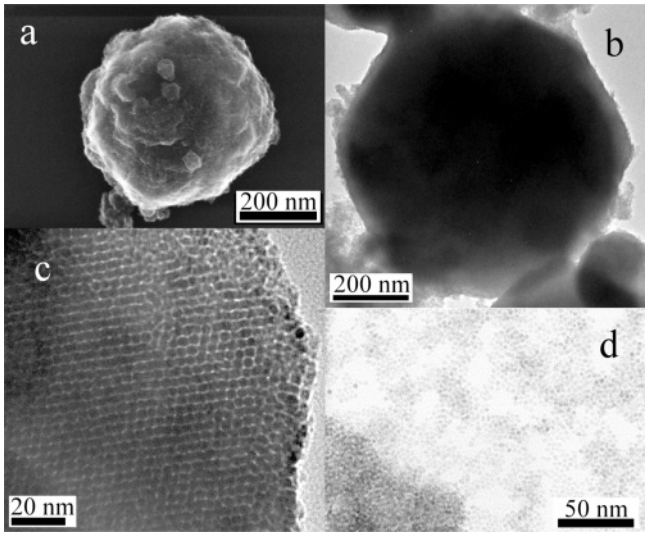

Figure 1. Electron micrographs of selected unannealed ZrO_2 colloidal: (a) SEM depicting a 500 nm-diameter, three-dimensional colloidal crystal; (b) similar TEM image depicting hexagonal faceting of the colloidal crystal; (c) magnified TEM of an edge of the colloidal crystal after flocculation depicting the HCP 4 nm diameter ZrO_2 nanoparticles components; and (d) TEM before flocculation but after removal of TOPO surfactants.

Results

Representative SEM and TEM images of unannealed ZrO_2 colloidal crystals are shown in parts a and b of Figure 1, respectively. While the TEM image (Figure 1b) depicts a single hexagonally faceted ZrO_2 crystal with small particulates along the edges, the SEM clearly shows the crystals (this one is 500 nanometers diameter) are three-dimensional and are composed of multiple layers of ordered ZrO_2 nanoparticles. The hexagonal faceting is not apparent in the SEM images, and smaller amorphous crystallites are found on the surface of the particle. Figure 1c shows an edge of a smaller ZrO_2 colloidal crystal. The individual 4 nm diameter nanoparticles are clearly discernible and monodisperse, and they adopt a hexagonal close packed structure. A very small size distribution of NPs is apparent (<5% diameter); otherwise, the assembly into a superlattice would not occur. Figure 1d shows the ZrO_2 nanoparticles after removal of the TOPO surfactants but before flocculation, indicating that raising the pH, not removing the surfactants, causes the nanoparticles to assemble into the superlattices. Figure 2 shows representative TEM images of the crystalline domains after

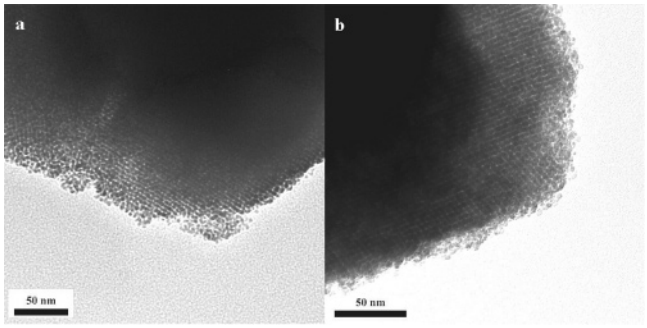

Figure 2. Electron micrographs of selected annealed ZrO_2 colloidal crystals. TEM of a (a) 300 °C and (b) 500 °C ZrO_2 colloidal crystal depicting the crystalline domains after heat treatment.

annealing at (a) 300 °C and (b) 500 °C, although amorphous regions that are difficult to observe are prevalent in the 500 °C sample. The reason these crystalline domains persist is not clear at present, although uncontrolled heating rates and insufficient temperatures may partially account for the inhomogeneity. Note the microscopic similarity of the crystalline domains to those of the unannealed sample in Figure 1c.

The adsorption−desorption isotherms of N_2 on unannealed ZrO_2 colloidal crystals demonstrated type III behavior with a small degree of hysteresis characteristic of weak adsorbate−adsorbent interactions commonly associated with multilayer adsorption onto either nonporous or microporous materials.[20,21] The BET surface area is 14.08 m^2/g, and a very broad pore size distribution is observed with a radius centered at 40 Å. In contrast, the adsorption−desorption isotherms of the zirconia colloidal crystals annealed at 300 °C exhibit type II behavior with a small degree of hysteresis, characteristic of multilayer adsorption onto micro- and mesoporous materials with relatively strong adsorbate−adsorbent interactions.[20,21] The specific surface area increased by a factor of 13 to 183.5 m^2/g due to the desorption of the water, CO_2, and residual organic material occupying the surfaces (as evidenced by TGA/MS) and interstitial spaces between the ordered ZrO_2 nanoparticles within the colloidal crystals, revealing a multitude of pores with a uniform pore size distribution at 4 Å while more broad distributions centered at 6 and 14 Å.

The small-angle X-ray scattering (SAXS) intensity profiles for the unannealed ZrO_2 colloidal crystals, as well as the samples sintered at 300, 350, 400, 450, and 500 °C, are shown in Figure 3. The complexity of the samples, which involve numerous length scales (i.e., the internanoparticle distances, on the order of nanometers, as well as the size of the colloidal crystals, on the order of micrometers) as well as ordering over relatively large domains, does not lend itself to the application of a single model for fitting the data, and thus, only a qualitative analysis is presented. The low-q data (up to 0.017 $Å^{-1}$) has a slope that ranges from −4.2 for the unannealed material to −4.5 for the sample sintered at 500 °C. These values suggest that the internal density of the colloidal crystals is not uniform, containing interstitial spaces and pores in agreement with the BET analysis. At room temperature, the scattering signatures are well-defined, suggesting the ZrO_2 nanoparticles assemble into a relatively ordered superlattice. The principal peak in the intensity is at 0.150 $Å^{-1}$ ($d = 4.2$ nm), which corresponds to the diameter of the NP components and correlates well with the diameter measured by TEM (∼4 nm). A broad and less intense second-order maximum is centered approximately at 0.25 $Å^{-1}$. The ratio of these two peak positions is $\sqrt{3}$, indicating a packing arrangement in agreement with an HCP lattice. Additionally,

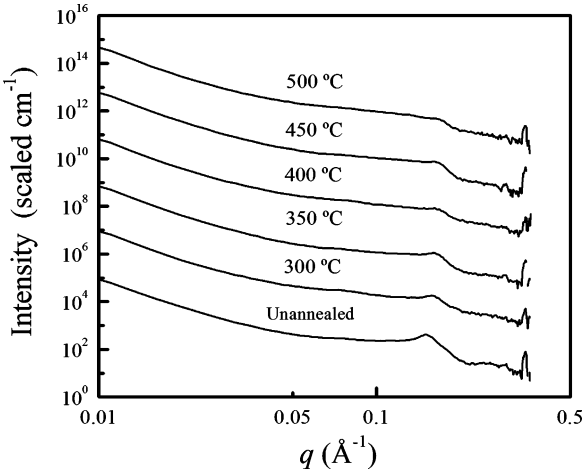

Figure 3. Small-angle X-ray scattering intensity plots of unannealed and annealed ZrO_2 colloidal crystals depict the shifting and gradual disappearance of the 4.2 nm reflection primary peak as the sample gradually becomes amorphous with increasing temperature.

TABLE 1: Position of the First Order SAXS Peak and *d* Spacing for the Various Annealing Temperatures

annealing temperature (°C)	peak position ($Å^{-1}$)	*d* spacing (Å)
unannealed	0.150	41.9
300	0.158	39.8
350	0.160	39.3
400	0.166	37.9
450	0.167	37.6
500	0.169	37.2

the widths of the two maxima are fairly broad, suggesting loose packing of the nanoparticles with no covalent or ionic bonding between the surfaces, which is expected for the unannealed sample. The primary peak is slightly asymmetric and broadened somewhat, consistent with a small particle size distribution. As the annealing temperature increases, the first-order peak decreases in intensity and moves to higher q values. Additionally, the second order reflection progressively disappears. The decrease in intensity indicates the sample becomes amorphous, but some ordered domains persist, as shown from the TEM images in Figure 2. The shift of the primary peak from 4.2 to 3.7 nm is consistent with the nanoparticle components packing closer. The first-order peak position as a function of temperature is tabulated in Table 1. The second-order peak, observed in the unannealed and 300 and 350 °C sintered samples, is replaced by a linear region in the samples heat treated at 400−500 °C on the log−log plot that has a slope of −1.84, averaged across the three data sets.

Variable-temperature in situ wide angle XRD measurements were also performed on the unannealed ZrO_2 colloidal crystals (Supporting Information). The temperature was ramped from 100 to 850 °C every 50 °C. At each temperature, a short scan was collected between 25° and 65° 2θ. The wide angle diffraction pattern encompassed the (111), (200), (220), and (311) peaks of zirconia.[14] The sharp peaks at 39.7° and 46.2° 2θ are from the Pt heating element. At low temperatures, the wide angle diffraction patterns correspond to tetragonal zirconia. The nanoscale domain size stabilizes the tetragonal phase due to the lower surface free energy compared to the monoclinic cell which is observed in the bulk solid.[22−24] From 100 to 750 °C, the (111), (220), and (311) peaks are unchanged. However, between 750 and 850 °C these peaks become noticeably sharper and more intense. The (200) peak intensity is too low to exhibit any noticeable feature changes with temperature. These changes

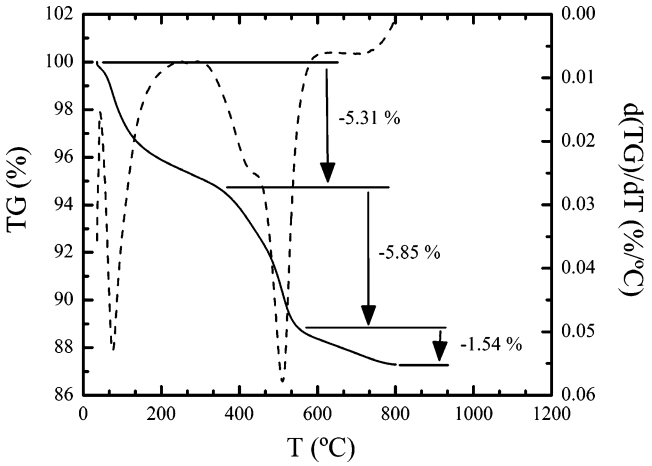

Figure 4. TGA plot of unannealed ZrO_2 colloidal crystals depicts the mass loss due to desorption of water, carbon dioxide, and residual organic molecules at high temperature. Dashed line (---) is first derivative of mass loss.

in peak character are attributed to a loss of nanoscale dimensions as the nanoparticles undergo a gradual ripening process to form bulk zirconia at 800 °C as well as a phase transition from the tetragonal to monoclinic phase.[14,17]

Thermogravimetric analysis of unannealed ZrO_2 colloidal crystals is shown in Figure 4 as the percent mass loss and corresponding derivative as a function of temperature. Typical mass spectral cycle reports for each corresponding mass loss step are provided in the Supporting Information. The TGA measurements indicate that approximately 12.75% of the original mass of the colloidal crystals is lost up to 800 °C in three distinct temperature regimes. From the onset of heating (first regime), water and CO_2 are initially lost by the sample. At higher temperatures (second and third regime), water and CO_2 continue to be desorbed as well residual organic material and SO_2 (from the sulfuric acid). The mass spectral analysis of the high-temperature regions indicates the presence of propylene and 2-chloropropane (byproducts of the zirconia isopropoxide and zirconia tetrachloride reaction), acetone and ethanol (solvents employed to wash the nanoparticles), and alkyl fragments from the TOPO surfactants. No decomposition products of the zirconia were detected in the experimental conditions.

Discussion

To assemble the zirconia nanoparticles into a superlattice, monodisperse nanoparticles were first synthesized and then stripped of the tri-*n*-octylphosphine oxide (TOPO) surfactants by refluxing the zirconia in an ethanol/water mixture containing a catalytic quantity of H_2SO_4. This treatment protonates the surface of the particles yielding a pH = 3.25 when the particles are redispersed in water. The pH of the dispersed nanoparticle solution was slowly raised by titrating with dilute KOH solution to a final pH of 7 which removes surface bound protons. This target pH is near the point-of-zero-charge (PZC) (5.5−5.8) [25,26] for zirconia whereby the particle surfaces are neutral and thus the solubility and interparticle repulsive forces are at a minimum. By concentrating the suspension, the nanoparticles can assemble into stable superlattices. Thus, by exploiting surface charge and solubility properties, micrometer-sized colloidal crystals of zirconia can easily be grown without utilizing hydrocarbon surfactants or solvents.

Following crystallization, the assembled monoliths were heat-treated at various temperatures (300−500 °C) to sinter the nanoparticles together in order to drive off excess water and form stable colloidal structures. The temperatures employed were not high enough to destroy the individual nanoscale character of each particle. The surfaces of the nanoparticles, now neutralized, are terminated with hydroxyl functionalities and in direct or close contact with one another. Over the course of heat treatment, water is lost, and a covalent oxide bridge is presumably formed between the nanoparticles. The heating also removes residual organic material and water trapped in the interstitial spaces between the nanoparticles, allowing a closer approach of the nanoparticle surfaces to pack together more efficiently while revealing a network of pores and interstitial spaces within the monoliths. Ali and Zaki[27] recently measured the conversion of zirconium hydroxide to zirconia at various temperatures, concluding that conversion begins to take place between 300 and 400 °C. During the conversion from zirconium hydroxide to zirconia, 2 mol of water is lost for each mole of zirconium hydroxide [$Zr(OH)_4 \rightarrow ZrO_2 + 2H_2O$], yielding oxide crystallization between adjacent zirconium atoms. Since the zirconium nanoparticles are oxide terminated, which they must be in order to be titrated effectively, it stands to reason that heat treatment of the nanoparticles will lead to dehydration of the particle surfaces and formation of crystalline zirconium oxide at each nanoparticle-nanoparticle interface. This is circumstantially supported by the shortening of the *d* spacing of the colloidal crystal with increasing temperature (Table 1) and the second loss of water and mass at ∼350 °C (TGA, Figure 4).

Although heating typically improves the crystallinity of solid-state materials, in this case heating above 350 °C appears to break down the colloidal crystals as the samples become progressively more amorphous (the individual nanoparticles remain intact to 750 °C). At high temperatures (>750 °C), the nanoparticles undergo a gradual ripening leading to the formation of bulk monoclinic ZrO_2. Between the temperatures of 350 and 750 °C, the regions that do remain crystalline appear using TEM to become more so (Figure 2b). We suspect that uncontrolled heating rates and insufficient heating temperatures and time may account for the loss of colloidal crystallinity with increasing temperature. However, the exact mechanism behind loss of crystallinity and the strategy to mitigate it are currently under investigation.

According to TEM, the nanoparticles have a diameter of approximately 4 nm. The *d* spacing according to SAXS is 4.2 nm for the unannealed colloidal crystals, decreasing to 3.7 nm at 500 °C. The *d* spacing should be a close approximation of the nanoparticle diameter plus any water or residual organic material on the particle. This shortening of the initial *d* spacing may be accommodated by either a shrinking of the nanoparticle caused by the dehydration of the outer zirconium hydroxide layer, or a highly efficient packing that exploits the surface morphology (faceting) of the nanoparticles. This process may be coupled to the loss in crystallinity; however, that has not been demonstrated.

Summary

Micrometer-sized zirconia colloidal crystals were synthesized in water without using hydrocarbon surfactants or solvents to facilitate crystal growth. With titration to the point-of-zero-charge, the nanoparticle solubility is minimized and the surfaces are neutralized, promoting assembly of the nanocomponents into ordered monoliths. Three-dimensional hexagonal faceted crystals were found to be composed of monodisperse 4 nm diameter ZrO_2 nanoparticles. Since no organic surfactants are present, the colloidal crystals are thermally stable and were further annealed at high temperatures (300−500 °C) to enhance

robustness. The annealing desorbs CO_2 and water trapped in interstitial spaces and pores. Above 350 °C, the sintering causes the samples to become amorphous, but some ordered domains of nanoparticles are retained after high temperature treatment. Thus, by exploiting surface charge and solubility properties, micrometer-sized colloidal crystals of zirconia with exceptional thermal stability can easily be grown without utilizing hydrocarbon surfactants or solvents.

Acknowledgment. Useful discussions of SAXS data interpretation with Dr. J. S. Lin are gratefully acknowledged. Research sponsored by the DOE Office of Basic Energy Sciences (OBES) and the DOE Office of Biological and Environmental Research (OBER). ORNL is managed by UT-Battelle, LLC for the U. S. Department of Energy under Contract No. DE-AC05-00OR22725. Electron microscopy performed at the ORNL High-Temperature Materials Laboratory.

Supporting Information Available: Wide-angle X-ray scattering and TGA-MS spectra. This material is available free of charge via the Internet at http://pubs.acs.org.

References and Notes

(1) Murray, C. B.; Kagan, C. R.; Bawendi, M. G. *Science* **1995**, *270*, 1335.
(2) Redl, F. X.; Cho, K. S.; Murray, C. B.; O'Brien, S. *Nature* **2003**, *423*, 968.
(3) Shevchenko, E. V.; Talapin, D. V.; O'Brien, S.; Murray, C. B. *J. Am. Chem. Soc.* **2005**, *127*, 8741.
(4) Saunders, A. E.; Korgel, B. A. *ChemPhysChem* **2005**, *6*, 61.
(5) Hunt, N.; Jardine, R.; Bartlett, P. *Phys. Rev. E* **2000**, *62*, 900.
(6) Schofield, A. B. *Phys. Rev. E* **2001**, *6405*, art. no.
(7) Wang, W.; Gu, B. *J. of Phys. Chem. B* **2005**, *109*, 22175.
(8) Murray, C. B.; Kagan, C. R.; Bawendi, M. G. *Ann. Rev. Mater. Sci.* **2000**, *30*, 545.
(9) Zeng, H.; Li, J.; Wang, Z. L.; Liu, J. P.; Sun, S. *Nano Lett.* **2004**, *4*, 187.
(10) Shevchenko, E. V.; Talapin, D. V.; Murray, C. B.; O'Brien, S. *J. Am. Chem. Soc.* **2006**, *128*, 3620.
(11) Caballero, J. B.; Puertas, A. M.; Fernandez-Barbero, A.; de las Nieves, F. J. *J. Chem. Phys.* **2004**, *121*, 2428.
(12) Leunissen, M. E.; Christova, C. G.; Hynninen, A. P.; Royall, C. P.; Campbell, A. I.; Imhof, A.; Dijkstra, M.; van Roij, R.; van Blaaderen, A. *Nature* **2005**, *437*, 235.
(13) Kalsin, A. M.; Fialkowski, M.; Paszewski, M.; Smoukov, S. K.; Grzybowski, B. A. *Science* **2006**, *312*, 420.
(14) Joo, J.; Yu, T.; Kim, Y. W.; Park, H. M.; Wu, F.; Zhang, J. Z.; Hyeon, T. *J. Am. Chem. Soc.* **2003**, *125*, 6553.
(15) Hassan, A. A. E.; Menzler, N. H.; Blass, G.; Ali, M. E.; Buchkremer, H. P.; Stover, D. *J. Mater. Sci.* **2002**, *37*, 3467.
(16) Mishra, M. K.; Tyagi, B.; Jasra, R. V. *Ind. Eng. Chem. Res.* **2003**, *42*, 5727.
(17) Shukla, S.; Seal, S.; Vij, R.; Brandyopadhyay, S.; Rahman, Z. *Nano Lett.* **2002**, *2*, 989.
(18) Hendricks, R. W. *J. Appl. Crystallogr.* **1978**, *11*, 15.
(19) Wignall, G. D.; Lin, J. S.; Spooner, S. *J. Appl. Crystallogr.* **1990**, *23*, 241.
(20) Kiselev, A. V. *J. Colloid Interface Sci.* **1968**, *28*, 430.
(21) Webb, P. A.; Orr, C. *Analytical Methods in Fine Particle Technology*, 1st ed.; Micromeritics Instrument Corporation: Norcross, GA, 1997.
(22) Baldinozzi, G.; Simeone, D.; Gosset, D.; Dutheil, M. *Phys. Rev. Lett.* **2003**, *90*, 216103.
(23) Chraska, T.; King, A. H.; Berndt, C. C. *Mater. Sci. Eng.* **2000**, *A286*, 169.
(24) Garvie, R. C. *J. Phys. Chem.* **1965**, *69*, 1238.
(25) Ghzaoui, A. E. *J. Appl. Phys.* **1999**, *86*, 5894.
(26) Zajac, J.; Lindheimer, M.; Partyka, S. *Colloids Surf., A* **1995**, *98*, 197.
(27) Ali, A. A. M.; Zaki, M. I. *Thermochim. Acta* **2002**, *387*, 29.